Published in final edited form as:
Med Eng Phys. 2012 April ; 34(3): 350–356. doi:10.1016/j.medengphy.2011.07.022.

Load/Strain Distribution between Ulna and Radius in the Mouse Forearm Compression Loading Model

Yunkai Lu[1], **Ganesh Thiagarajan**[1], **Daniel P. Nicolella**[2], and **Mark L. Johnson**[3]

[1]Department of Civil and Mechanical Engineering, University of Missouri-Kansas City, 350L Flarsheim Hall, 5100 Rockhill Road, Kansas City, MO 64110

[2]Mechanical Engineering Division, Southwest Research Institute, 6220 Culebra Road, San Antonio, TX 78238

[3]School of Dentistry, University of Missouri-Kansas City, Room 3143, 650 E 25thStreet, Kansas City, MO 64108

Abstract

Finite element analysis (FEA) of the mouse forearm compression loading model is used to relate strain distributions with downstream changes in bone formation and responses of bone cells. The objective of this study was to develop two FEA models – the first one with the traditional ulna only and the second one in which both the ulna and radius are included, in order to examine the effect of the inclusion of the radius on the strain distributions in the ulna. The entire mouse forearm was scanned using microCT and images were converted into FEA tetrahedral meshes using a suite of software programs. The performance of both linear and quadratic tetrahedral elements and coarse and fine meshes were studied. A load of 2 N was applied to the ulna/radius model and a 1.3 N load (based on previous investigations of load sharing between the ulna and radius in rats) was applied to the ulna only model for subsequent simulations. The results showed differences in the cross sectional strain distributions and magnitude within the ulna for the combined ulna/radius model versus the ulna only model. The maximal strain in the combined model occurred about 4 mm towards the distal end from the ulna mid-shaft in both models. Results from the FEA model simulations were also compared to experimentally determined strain values. We conclude that inclusion of the radius in FE models to predict strains during *in vivo* forearm loading increases the magnitude of the estimated ulna strains compared to those predicted from a model of the ulna alone but the distribution was similar. This has important ramifications for future studies to understand strain thresholds needed to activate bone cell responses to mechanical loading.

Keywords

Ulna; Radius; Finite Element Analysis; Mechanical Load; Mouse Model

Address all correspondence to: ganesht@umkc.edu, Ph: (816)-235-1288 Fax: (816)-235-1260.

Introduction

The *in vivo* forearm compressive loading model is widely used to study bone formation in response to mechanical loading [1-10]. In vivo mouse forearm compression loading experiments are typically conducted by applying a cyclic load that produces a particular maximum bone surface strain in the ulna. The desired surface strain is achieved by calibrating load levels using a strain gage attached to the ulna surface and then applying different magnitudes of loads to determine the resultant strain and displacement values. In order to understand the mechanisms by which *in vivo* forearm loading may be triggering an osteogenic response, finite element analysis (FEA) models have been constructed to assess general strain distributions within the bone tissue that result from the applied external mechanical loading. FEA models of the mouse tibia [11, 12], rat ulna [13-15] and turkey ulna [16] have all been described by various researchers. However, the mouse ulna models generally do not include the radius, and consequently use estimates of load sharing between the ulna and radius for model boundary conditions to predict strain distributions within the ulna. These estimated strain distributions are commonly used to assess the relationship between mechanical stimulation and the osteogenic response in bone. Silva et al [12] used a tibia-fibula FEA model for simulating their three point bending experiments.

Osteocytes located within the bone matrix appear to respond to load in a heterogeneous manner. It was originally hypothesized [17] that Lrp5 and the Wnt/β-catenin signaling pathway were involved in bone responsiveness to mechanical loading. This has been confirmed in a number of studies from our lab and other investigators [18-21]. Recent findings in our laboratory have shown that activation of β–catenin signaling in bone in response to mouse forearm compression mechanical loading occurs first in osteocytes and then propagates to surrounding osteocytes and eventually to cells on the bone surfaces where new bone formation will occur [22]. However, within a given uniform strain field as predicted by finite element analysis (FEA), not all osteocytes activate β–catenin signaling, even ones that are adjacent to each other [22] demonstrating a heterogeneous response. Nicolella et al.[23] have previously shown that the strain fields in bone slices around osteocytes can vary dramatically within a relatively small spatial region. This heterogeneity in the osteocyte response suggested to us that the current FEA models of the ulna do not adequately capture the strain fields at this microscale level. In order to eventually achieve that goal, the purpose of this study was to lay down a foundation by constructing a first generation FEA model of the mouse forearm that included both the ulna and radius, called the Ulna Radius Model (URM), and compare load sharing, strain magnitudes and distributions with a corresponding Ulna only Model (UM).

2. Methods

2.1. Finite Element Modeling

Finite element models of a TOPGAL mouse forearm were developed from MicroCT images with a 65 μm resolution in plane and the axial slices were 12 μm apart (Scanco MicroCT, Scanco Medical, Basserdorf, Switzerland). The TOPGAL mouse was used so that future studies can be performed comparing the osteocyte biological response with magnitude of strain at the cellular level. This mouse is normal except for expression of a reporter for activation of the β-catenin pathway [24]. The microCT (μCT) scan images (1100 slices) were imported into Slicer3D v3.2.1 (www.slicer.org) [25, 26] where both the endosteal and periosteal cortical boundary of each bone were manually traced. The resulting segmented images were imported into GeoMagic Studio 9 (www.geomagic.com) where the 3D object underwent smoothing, patching, curve-fitting, and surface mapping before the final CAD model was created.

Meshing was performed using an automatic mesh generation process using ABAQUS v6.10-1 CAE using tetrahedron elements. Both four node and ten node tetrahedron elements were each used to generate two different mesh densities (coarse mesh and fine mesh) that were subsequently used to investigate finite element solution convergence (mesh convergence). The ulna plus radius coarse mesh was constructed using ten node tetrahedral elements and had 19,550 nodes and 11,405 elements. Its counterpart, the fine mesh with ten node tetrahedral elements had 192,674 nodes and 124,145 elements. On the other hand, the coarse four node tetrahedral mesh had 6,048 nodes and 23,818 elements and the fine mesh with four node tetrahedral elements had 27,468 nodes and 124,145 elements.

Before the static analysis was conducted, a coordinate transformation was applied to the model such that the ulna was aligned in the vertical direction (*z*-axis) in order to be consistent with the alignment of the ulna during *in vivo* loading experiments. The model loading boundary conditions consisted of a concentrated load of 2 N along the *z*-axis applied at the proximal end of ulna. A fixed boundary condition was imposed on selected nodes at the distal end of both the ulna and radius. Linear one dimensional spring elements were used to simulate the ligament that connects the ulna and radius at both the ends of the radius. A spring constant of 1400 N/mm was used [27]. While we did not explicitly determine the spring constant for this study, Silva et al [12] compared models with rigid fusion and no constraint between the tibiofibular joint and found that the difference in strain values at the mid-diaphysis region was only three percent.

2.2. Material Properties of Bone

A wide range of values for the mechanical properties, especially the elastic modulus and density, of rat and mouse bones have been reported [28-35] in literature. For instance, the elastic modulus of the femur was experimentally determined to range from 8 GPa to 34 GPa by bending tests [14, 36] or through nano-indentation technique [30, 34, 37-39].

Although no experimentally obtained data for the biomechanical properties of the mouse ulna/radius used in this study were available, we assigned an elastic modulus of 20 GPa to ulna and 18 GPa to radius in our FE analysis based on the values reported in the literature [12]. The cortical bone mineral density determined by μCT of the mouse forearm used to generate the models was 1168 kg/m^3 for the ulna and 1172 kg/m^3 for the radius, and Poisson's ratio was set at 0.30 and 0.33 for ulna and radius, respectively.

The final finite element models were imported into two commercially available FEA programs (ABAQUS v 6.10-1 [Simulia, Providence, RI], and LS-DYNA v971 [LSTC Inc., Livermore, CA]) to conduct the FE analyses/simulations. For LS-DYNA element formulation number 10 (4-noded tetrahedron with 1 integration point) was used for the four node tetrahedral and element formulation 16 (10-noded tetrahedron with 4 or 5 integration points) was used for the 10 node tetrahedral mesh. The exact same load and boundary conditions were applied for each analysis performed with each program.

2.3. Ex vivo Strain Gaging

Forearm experimental data using TOPGAL mice were obtained from ex vivo loading using the Bose ElectroForce 3220 system. Maximum compressive strains were measured using a strain gage (Vishay EA-06-015DJ-120/LE) applied to the ulna (at 2 mm distal to the ulna mid-shaft on the medial surface and at a site 5 mm distal to the end of the olecranon process on the lateral surface). The forearms were kept hydrated with phosphate buffered saline throughout the measurements. After application of strain gage, loading was conducted on the right forearm at 2 Hz, using a haversine waveform for 15 cycles. Loading is conducted at

0.7, 1.2, 1.7, 2.2, 2.7 and 3.1 N for the intact forearm. Strains in the last five cycles were averaged.

3. Results

3.1. Model Validation

Figure 1 shows the displacement contours calculated using ABAQUS and LS-DYNA. The contour profiles determined by both methods demonstrate a high degree of similarity. Maximum displacements predicted by each model are compared directly in Table 1 for the two FEA codes using each type of mesh. Overall, there was very good agreement between these programs. Using ABAQUS, the difference between the coarse mesh maximum displacement (0.167 mm for the 10 noded tetrahedron) and the corresponding fine mesh value (0.183mm) was 11.36% despite increasing the number of elements 10.89 fold. Models constructed using the quadratic 10-node tetrahedron element (ABAQUS and LS-DYNA) predicted larger deformation (0.1833 and 0.1810 mm, respectively) compared to their 4-node counterpart (0.1183 and 0.1436 mm, respectively). In order to check the sensitivity of the displacement values to the differences in the elastic modulus of the ulna and radius (20 GPa and 18 GPa) and Poisson's ratio (0.3 and 0.33) several combinations were run and the difference in displacement values was less than one percent.

However, the principal stress and strain values showed a higher percentage of difference between the fine and coarse mesh models. At an almost identical location the maximum axial stress values were 71 MPa and 52.8 MPa in compression for the fine and coarse meshes respectively and the axial strain values were 3510 and 2613 microstrain respectively. The stress and strain values are slower to converge compared to displacements. A difference of about 25% was observed in both the stress and strain values at approximately identical locations.

3.2. Load Distribution Between Ulna/Radius

Our goal was to investigate the influence of the inclusion of the radius on the load distribution between ulna and radius. The resutling force at the mid shaft region of the URM and UM were calculated by making a cross sectional cut using LS-DYNA. Table 2 shows the distribution of forces, which can be readily found from the postprocessing module of LSDYNA, in the axial direction for all the cases. The percentage of load shared by the ulna for the 10 node coarse and fine mesh was 87.3 and 71.2 respectively. For the 4 node coarse and fine mesh the values were 87.0 and 64.9 percent respectively.

3.3. Strain Distribution

The strain distribution is of great interest as it is commonly hypothesized that bone formation is triggered as a direct result of *local* strain within the bone matrix applied during loading. In practice a strain gage is attached to the surface of the ulna and a load is applied that will generate an osteogenic strain (generally >1500 microstrain). Since the load is applied at the proximal end, the combined compressive load and the bending moment causes the lateral side of the ulna to experience mostly tensile strains and medial side mostly compressive strains. A load of 2 N was used in the FE analysis and was applied at the proximal end. Kotha et al. (2004) previously reported, in the rat ulnar loading model, that the ulna carries 65% of the load, which is in agreement with our 4 and 10 node fine mesh values. We applied a load of 1.3 N (65% of 2 N) to the UM and compared the results with those of the ulna in the URM subjected to 2 N load. Figure 2 shows the axial strain variation along the periosteal surface at the mid-shaft of the ulna for both the URM and UM. The cross section contour plots of axial strain at the same location for the URM and the UM are displayed in Figure 3. The tensile strain distribution in the URM ranges from 1263-1800

microstrain while the tensile strain in the UM ranges from 725-1263 microstrain. The compressive strains are also higher in the URM (1425-1962 microstrain) compared to UM (887-1425 microstrain).

Additionally the FEA models enable us to examine maximum axial strains on a cross-sectional slice at any point along the ulna for both URM and UM. Slices were taken at 1 mm apart from mid-shaft of the ulna toward both distal and proximal ends. The peak compressive and tensile strain values at each cross section were extracted and the results are shown in Figure 4. Figure 4 also includes the peak compressive and tensile strain values at each cross section, for the UM model with 65% of the load. The maximum compressive and tensile strains in the overall ulna for the URM and the UM model loaded with 65% of the load are shown in Table 3. The solid lines, in Figure 4, represent the peak tensile and compressive strains on the ulna along the proximal-distal direction for the URM model and the dotted lines represent the same for the UM model. These data indicate that; a) the peak strains in both the URM and UM occur at about 4 mm distal to the midshaft, b) the peak tensile strains for the URM and UM are 2229 and 1732 microstrain and c) the peak compressive strains for the URM and UM are 2986 and 2356 microstrain, respectively.

3.4. Experimental Comparison

In order to present a preliminary validation of the model, we performed simulations using loads varying from 1 N to 3.5 N at 0.5 N increments applied to the URM model and the UM model loaded with 65% of the load. A comparison of the maximal compressive and tensile strains from the numerical simulations and experimental strain gage study is shown in Figure 5. These data demonstrated that the predicted axial strains from the UM model are lower than the experimentally obtained data, while values from the URM model are slightly higher.

4. Discussions

The *in vivo* forearm compression loading model is widely used in the bone biology field as a method for examining changes in bone formation in response to load as well as determining the mechanisms mediating the responses of loading on osteoblast and osteocytes. For example in an early study by Lanyon and colleagues [40], they demonstrated rapid changes in glucose-6-phosphate dehydrogenase activity in osteocytes in response to loading. Recently, Robling et al.[21] used *in situ* hybridization and immunostaining to correlate changes in specific gene expression with bone formation. In order to understand how loading activates cellular response pathways, a more precise model of the actual strain levels that the osteocytes experience is needed. Harris et al. [41] determined that activation of Dentin Matrix Protein 1 (DMP1) gene expression, which is expressed in osteocytes and is known to be involved in bone mineralization, required a minimum compressive strain of 1500 microstrain. This threshold was achieved along the length of the ulna from a point just proximal to the midshaft to a point ~ 4mm distal. Interestingly their model predicted a maximum strain at ~3-4 mm distal to the midshaft, which coincided with maximal DMP1 expression [41, 42]. However, Zhang et al [43] reported maximal *E11* expression in response to forearm loading in a region 1-3mm proximal to the midshaft. The fact that different genes appear to activate in different regions of the ulna and do not directly correlate with FE based predicted maximal strains might seem paradoxical. However there are two important considerations in interpreting these data; 1) the models we present and those previously published, only provide estimates of global strain, not cell or micro-level strains, and 2) if a correction factor is not applied, the UM model may underestimate the strain magnitude, not necessarily the distribution, needed to initiate a biological response. Alternatively, one gene may be involved in bone formation (DMP1) and the other in bone resorption (*E11*) suggesting again that different magnitudes of strain are translated into

either signals of formation or resorption. Therefore it appears that FE models built at a higher level of resolution are required, specifically at the osteocyte level, in order to better understand how strain correlates with changes in gene expression. We are currently developing strain maps with an osteocyte level of resolution based upon the URM FE modeling presented in this manuscript.

Inclusion of the radius in the modeling effort is critical for a number of reasons. First, it is a more realistic representation of how *in vivo* experiments are conducted. While it can be argued that the current model does not include some of the other elements present such as the phalanges, muscle connectivity etc., the URM model presented here is probably the first attempt, to the best of our knowledge, to include the radius in a modeling effort. Secondly, the URM allows for the kinematics of the ulna to be driven by the presence of the radius, and incorporates the boundary conditions of contact between the ulna and radius as well. Also, when the forearm is loaded biological responses can be expected to occur in both the ulna and radius and this model enables us to simultaneously investigate the relationship of strain to responses in both bones. Our data clearly show different strain distributions in the cross sections from the UM and URM and the peak strain values, in both tension and compression, are higher in the URM model compared to the UM model. Ultimately we want to determine the osteocyte strain threshold for activation of a response to loading, which is critical for the design of appropriate loading regimens that will induce new bone formation, especially as the material properties of bone, which may change with aging or upon drug treatment, etc., are factored into the analysis.

By studying two mesh sizes and two types of element formulations we demonstrated that if a second order tetrahedron element is used in the mesh generation, even a coarse mesh will yield results that are close to the fine mesh values. This is consistent with the study of Ramos and Simões [44] in which hexahedral and both linear and quadratic tetrahedral elements were used to mesh human proximal femur and it was concluded that the results between the meshes did not show any significant differences. Therefore, higher order element formulation proved to be very efficient in meshing bone structures and this saves computational time.

In our models the maximal resultant displacement occurred close to the mid-shaft of ulna with or without the radius in the analysis. The deformation data indicated that for the specific type of boundary and loading conditions, the ulna takes 65-87% of the total applied load. Not surprisingly we found that the stiffer models with a coarse mesh resulted in a higher percentage of load shared by the ulna. In a previous study, Kotha et al.[13] estimated that the ulna encumbered 65% of the load. We obtained a similar result from our 4- and 10-node fine mesh models. The absolute value of strain is a critical value for studies that attempt to determine a strain threshold for activation of a particular biological response [41]. Our data indicate that the choice of model is a critical determinant of the strain threshold value.

Several findings in this study are also consistent with previously published reports. The strain field is caused by a combination of compressive load and bending moments. The maximal strain locations do not occur right at the mid-shaft of the ulna/radius as seen in Figure 4. For the models under study, the peak values are located about 4 mm to the distal end from the mid-shaft. The maximal compressive strain value (absolute) is about 1.5 times that of the tensile strain for both the URM and UM cases. However, differences in axial strain values of up to 26.4% were observed between the two approaches. Also as shown in Figure 5, the maximal strain values from FEA URM exceed those from the strain gage readings, which confirms that the strain gages measure the overall “averaged” strain across the surface of the bone where they are attached. Due to the small length of the mouse

forearm (15 mm or less), it is not surprising that the strain gage is not able to provide localized strain distribution information. The similarities of our findings with previously published data highlight that the differences we did observe between the URM and UM models are important considerations for future studies using FEA in the bone field.

We evaluated the use of the ulna only in the FEA under the assumption of a fixed 65% load carrying (Figure 5). In Figure 5 it can be seen that the predicted maximal strain on the ulna in the URM is 25% higher than the value predicted using the FEA UM model. Hence, the full forearm URM model presented in this study appears to predict more closely the strain values along the bone surfaces as compared with models that include only the ulna in the analysis, unless a correction factor is applied to the UM model to bring it into alignment with the URM model.

Our current modeling does have its limitations. First, we need to model the tissue contacts between the radius and ulna using simple springs and the spring constant for this needs to be determined. Secondly, the muscle and other bones of the forearm (humerus and paw bones) are not yet included and their contribution to the ulna strain fields is not known. Thirdly, the boundary conditions of the loading caps are more complex than what we have incorporated into this first generation FEA URM. Finally, the osteocyte lacunae and vascular canals in bone act as strain concentrators and the material properties of bone are not homogeneous [23]. To overcome these issues models are currently being built from μCT and higher resolution images of statically loaded bones at various load levels to adjust the URM models to match actual displacements.

In conclusion, we have constructed and compared different FEA models of strain distributions in the mouse forearm under compressive loading. We observed that the approach used to construct the FEA model significantly altered the predicted strain distributions and the amount of load shared by the ulna versus radius varied considerably amongst models. We found that a tetrahedral ten node coarse mesh model was capable of predicting strain distributions that are in good agreement with experimental values. Finally inclusion of the radius in the FEA model resulted in significant changes in the peak strain and distribution of strain within the ulna, strongly suggesting that this type of FEA model is needed to fully understand how load applied to the forearm correlates to changes in bone's response to mechanical loading.

Acknowledgments

The project was funded by a grant from the National Institutes of Health – NIAMS R01 AR053949 (ML Johnson) and NIAMS P01 AR46798 (LF Bonewald PI, ML Johnson co-I) and by the Missouri Life Science Research Board and UMKC Center of Excellence in Mineralized Tissues (ML Johnson and G Thiagarajan). The authors thank Mr. Mark Dallas for his expert technical assistance with the loading aspects of these studies and Dr. Lynda Bonewald for her critical review of the manuscript.

References

1. Perry MJ, Parry LK, Burton VJ, Gheduzzi S, Beresford JN, Humphrey VF, et al. Ultrasound mimics the effect of mechanical loading on bone formation *in vivo* on rat ulnae. Medical Engineering & Physics. 2009; 31:42–7. [PubMed: 18495517]
2. Hsieh YF, Wang T, Turner CH. Viscoelastic response of the rat loading model: implications for studies of strain-adaptive bone formation. Bone. 1999; 25:379–82. [PubMed: 10495144]
3. Rubin C, Lanyon L. Regulation of bone formation by applied dynamic loads. J Bone Joint Surg Am. 1984; 66:397–402. [PubMed: 6699056]
4. Mosley JR, Lanyon LE. Strain rate as a controlling influence on adaptive modeling in response to dynamic loading of the ulna in growing male rats. Bone. 1998; 23:313–8. [PubMed: 9763142]

5. Robling AG, Duijvelaar KM, Geevers JV, Ohashi N, Turner CH. Modulation of appositional and longitudinal bone growth in the rat ulna by applied static and dynamic force. Bone. 2001; 29:105–13. [PubMed: 11502470]
6. Torrance AG, Mosley JR, Suswillo RFL, Lanyon LE. Noninvasive loading of the rat ulna *in vivo* induces a strain-related modeling response uncomplicated by trauma or periostal pressure. Calcified Tissue International. 1994; 54:241–7. [PubMed: 8055374]
7. Uthgenannt BA, Silva MJ. Use of the rat forelimb compression model to create discrete levels of bone damage *in vivo*. Journal of Biomechanics. 2007; 40:317–24. [PubMed: 16519891]
8. Lanyon LE. Osteocytes, strain detection, bone modeling and remodeling. Calcified Tissue International. 1993; 53:S102–S7. [PubMed: 8275362]
9. Hillam RA, Skerry TM. Inhibition of bone resorption and stimulation of formation by mechanical loading of the modeling rat ulna *in vivo*. Journal of Bone and Mineral Research. 1995; 10:683–9. [PubMed: 7639102]
10. Hsieh YF, Silva MJ. In vivo fatigue loading of the rat ulna induces both bone formation and resorption and leads to time-related changes in bone mechanical properties and density. Journal of Orthopaedic Research. 2002; 20:764–71. [PubMed: 12168665]
11. Gross TS, Srinivasan S, Liu CC, Clemens TL, Bain SD. Noninvasive loading of the murine tibia: an *in vivo* model for the study of mechanotransduction. J Bone Miner Res. 2002; 17:493–501. [PubMed: 11874240]
12. Silva MJ, Brodt MD, Hucker WJ. Finite element analysis of the mouse tibia: Estimating endocortical strain during three-point bending in SAMP6 osteoporotic mice. The Anatomical Record Part A: Discoveries in Molecular, Cellular, and Evolutionary Biology. 2005; 283A:380–90.
13. Kotha SP, Hsieh YF, Strigel RM, Müller R, Silva MJ. Experimental and finite element analysis of the rat ulnar loading model--correlations between strain and bone formation following fatigue loading. Journal of Biomechanics. 2004; 37:541–8. [PubMed: 14996566]
14. Tami AE, Nasser P, Schaffler MB, Tate MLK. Noninvasive fatigue fracture model of the rat ulna. Journal of Orthopaedic Research. 2003; 21:1018–24. [PubMed: 14554214]
15. Lynch JA, Silva MJ. In vivo static creep loading of the rat forelimb reduces ulnar structural properties at time-zero and induces damage-dependent woven bone formation. Bone. 2008; 42:942–9. [PubMed: 18295561]
16. Gross TS, Edwards JL, McLeod KJ, Rubin CT. Strain gradients correlate with sites of periosteal bone formation. J Bone Miner Res. 1997; 12:982–8. [PubMed: 9169359]
17. Bonewald LF, Johnson ML. Osteocytes, mechanosensing and Wnt signaling. Bone. 2008; 42:606–15. [PubMed: 18280232]
18. Robinson JA, Chatterjee-Kishore M, Yaworsky PJ, Cullen DM, Zhao W, Li C, et al. Wnt/β-Catenin Signaling Is a Normal Physiological Response to Mechanical Loading in Bone. Journal of Biological Chemistry. 2006; 281:31720–8. [PubMed: 16908522]
19. Lau KHW, Kapur S, Kesavan C, Baylink DJ. Up-regulation of the Wnt, Estrogen Receptor, Insulin-like Growth Factor-I, and Bone Morphogenetic Protein Pathways in C57BL/6J Osteoblasts as Opposed to C3H/HeJ Osteoblasts in Part Contributes to the Differential Anabolic Response to Fluid Shear. Journal of Biological Chemistry. 2006; 281:9576–88. [PubMed: 16461770]
20. Sawakami K, Robling AG, Ai M, Pitner ND, Liu D, Warden SJ, et al. The Wnt Co-receptor LRP5 Is Essential for Skeletal Mechanotransduction but Not for the Anabolic Bone Response to Parathyroid Hormone Treatment. Journal of Biological Chemistry. 2006; 281:23698–711. [PubMed: 16790443]
21. Robling AG, Niziolek PJ, Baldridge LA, Condon KW, Allen MR, Alam I, et al. Mechanical Stimulation of Bone in Vivo Reduces Osteocyte Expression of Sost/Sclerostin. Journal of Biological Chemistry. 2008; 283:5866–75. [PubMed: 18089564]
22. Kim-Weroha NAFA, Holladay B, Kotha SP, Kamel MA, Johnson ML. In vivo Load Activated Propagation of b-catenin Signaling in Osteocytes through Coordinated Downregulation of Inhibitors of Lrp5. J Bone Min Res. 2008; 23
23. Nicolella DP, Moravits DE, Gale AM, Bonewald LF, Lankford J. Osteocyte lacunae tissue strain in cortical bone. Journal of Biomechanics. 2006; 39:1735–43. [PubMed: 15993413]

24. DasGupta R, Fuchs E. Multiple roles for activated LEF/TCF transcription complexes during hair follicle development and differentiation. Development. 1999; 126:4557. [PubMed: 10498690]
25. Pieper S, Halle M, Kikinis R. 3D Slicer. Biomedical Imaging: Nano to Macro, 2004 IEEE International Symposium on 2004. 1:632–5.
26. Pieper S, Lorensen B, Schroeder W, Kikinis R. The NA-MIC Kit: ITK, VTK, pipelines, grids and 3D slicer as an open platform for the medical image computing community. Biomedical Imaging: Nano to Macro, 2006 3rd IEEE International Symposium on 2006. :698–701.
27. Donahue TLH, Hull ML, Rashid MM, Jacobs CR. A Finite Element Model of the Human Knee Joint for the Study of Tibio-Femoral Contact. Journal of Biomechanical Engineering. 2002; 124:273–80. [PubMed: 12071261]
28. Jämsä T, Rho JY, Fan Z, MacKay CA, Marks SC, Tuukkanen J. Mechanical properties in long bones of rat osteopetrotic mutations. Journal of Biomechanics. 2002; 35:161–5. [PubMed: 11784534]
29. Akhter MPFZ, Rho JY. Bone intrinsic material properties in three inbred mouse strains. Calcified Tissues International. 2004; 75:416–20.
30. Silva MJ, Brodt MD, Fan Z, Rho JY. Nanoindentation and whole-bone bending estimates of material properties in bones from the senescence accelerated mouse SAMP6. Journal of Biomechanics. 2004; 37:1639–46. [PubMed: 15388305]
31. Umeno T, Hara T, Endo N. Fragility of Vertebral Trabecular Bone Under Various Loading Orientations in Ovariectomized (OVX) Rats. Journal of Biomechanics. 2007; 40:S594–S.
32. Vanleene M, Rey C, Ho Ba Tho MC. Relationships between density and Young's modulus with microporosity and physico-chemical properties of Wistar rat cortical bone from growth to senescence. Medical Engineering & Physics. 2008; 30:1049–56. [PubMed: 18406196]
33. Nazarian A, Entezari V, Vartanians V, Müller R, Snyder BD. An improved method to assess torsional properties of rodent long bones. Journal of Biomechanics. 2009; 42:1720–5. [PubMed: 19447390]
34. Sun, Lw; Fan, Yb; Li, Dy; Zhao, F.; Xie, T.; Yang, X., et al. Evaluation of the mechanical properties of rat bone under simulated microgravity using nanoindentation. Acta Biomaterialia. 2009; 5:3506–11. [PubMed: 19450712]
35. Robling A, Turner C. Mechanotransduction in bone: genetic effects on mechanosensitivity in mice. Bone. 2002; 31:562–9. [PubMed: 12477569]
36. Leppänen O, Sievänen H, Jokihaara J, Pajamäki I, Järvinen TL. Three-Point Bending of Rat Femur in the Mediolateral Direction: Introduction and Validation of a Novel Biomechanical Testing Protocol. Journal of Bone and Mineral Research. 2006; 21:1231–7. [PubMed: 16869721]
37. Oliver W, Pharr G. An improved technique for determining hardness and elastic modulus using load and displacement sensing indentation experiments. Journal of Material Research. 1992; 7:1564–83.
38. Norman J, Shapter JG, Short K, Smith LJ, Fazzalari NL. Micromechanical properties of human trabecular bone: A hierarchical investigation using nanoindentation. Journal of Biomedical Materials Research Part A. 2008; 87A:196–202. [PubMed: 18085652]
39. Fan ZF, Smith P, Rauch F, Harris GF. Nanoindentation as a means for distinguishing clinical type of osteogenesis imperfecta. Composites Part B: Engineering. 2007; 38:411–5.
40. Dodds RA, Ali N, Pead MJ, Lanyon LE. Early loading-related changes in the activity of glucose 6-phosphate dehydrogenase and alkaline phosphatase in osteocytes and periosteal osteoblasts in rat fibulae *in vivo*. Journal of Bone and Mineral Research. 1993; 8:261–7. [PubMed: 8456583]
41. Harris S, Gluhak-Heinrich J, Harris M, Yang W, Bonewald L, Riha D, et al. DMP1 and MEPE expression are elevated in osteocytes after mechanical loading *in vivo*: Theoretical role in controlling mineral quality in the perilacunar matrix. Journal of Musuloskeletal and Neuronal Interactions. 2007; 7:313.
42. Yang W, Lu Y, Kalajzic I, Guo D, Harris MA, Gluhak-Heinrich J, et al. Dentin Matrix Protein 1 Gene Cis-regulation. Journal of Biological Chemistry. 2005; 280:20680. [PubMed: 15728181]
43. Zhang K, Barragan-Adjemian C, Ye L, Kotha S, Dallas M, Lu Y, et al. E11/gp38 selective expression in osteocytes: regulation by mechanical strain and role in dendrite elongation. Molecular and cellular biology. 2006; 26:4539. [PubMed: 16738320]

44. Ramos A, Simões JA. Tetrahedral versus hexahedral finite elements in numerical modelling of the proximal femur. Medical Engineering & Physics. 2006; 28:916–24. [PubMed: 16464628]

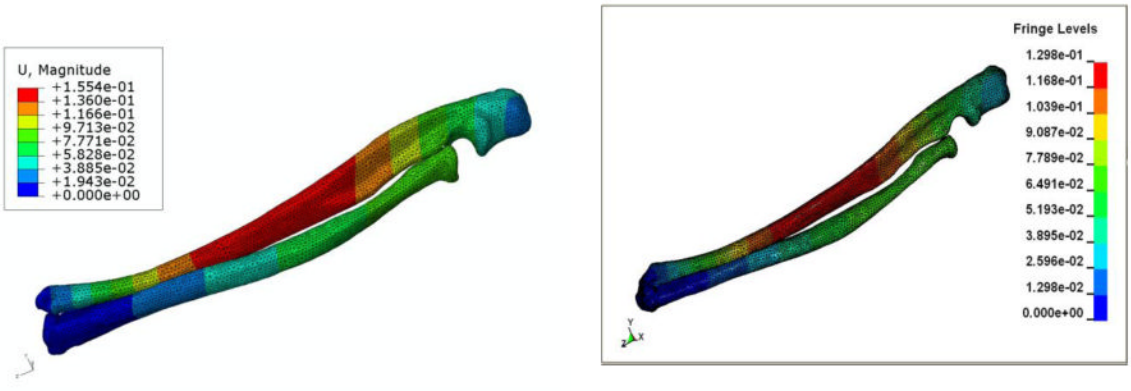

Figure 1.
Images showing the displacement contours (in mm – using 10 node fine mesh) from the ulna radius model (URM) using ABAQUS (left), and LS-DYNA (right). The URM was subjected to constant axial load of 2 N.

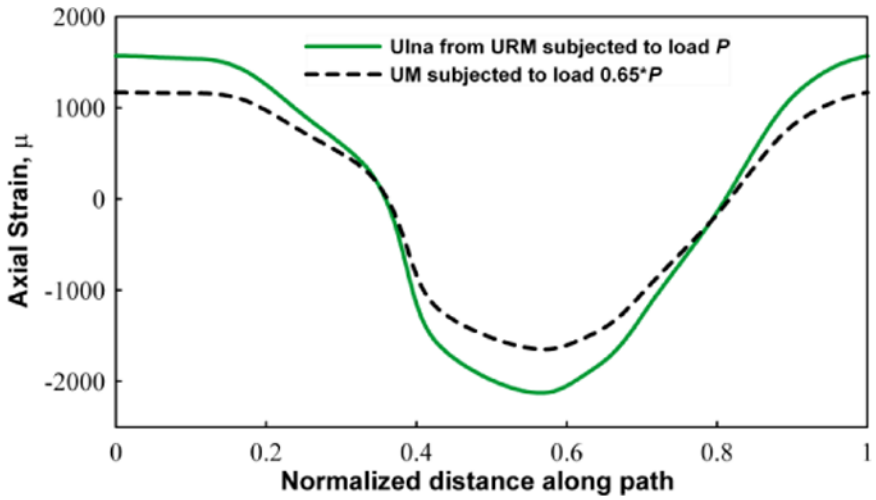

Figure 2.

Graph showing the variation of the *z*-direction strain (using 10 node fine mesh) around a circumferential path on the surface of ulna. The section is taken at the mid shaft region. The graph shows the comparison of the strain for the URM with a full 2 N load and the corresponding UM with 1.3 N (65%) load. Tensile and compressive strains are observed, as expected, in the medial and lateral sides of the ulna.

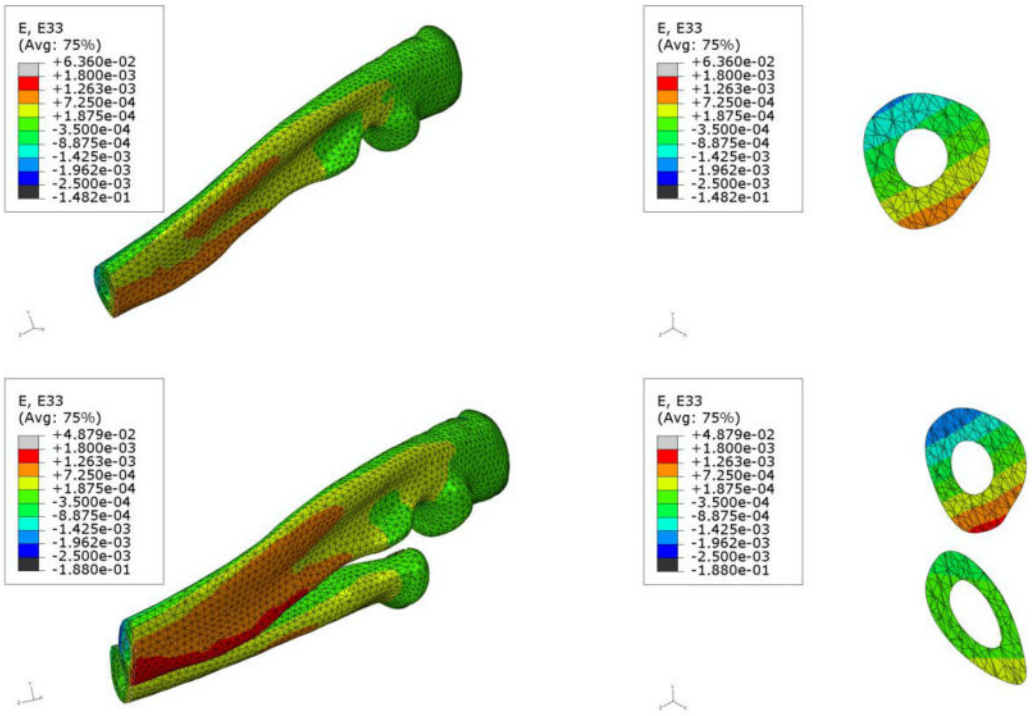

Figure 3.
Comparative images showing the z-direction strain contours (using 10 node fine mesh) on one half of the ulna in the UM (top) and the ulna and radius in the URM (bottom). The URM was subjected to 2 N axial force while the UM was subjected to 1.3 N axial force. From the images on the right hand side of each row, it can be clearly seen that the ulna in the URM experiences higher tensile stresses compared to the ulna in the UM.

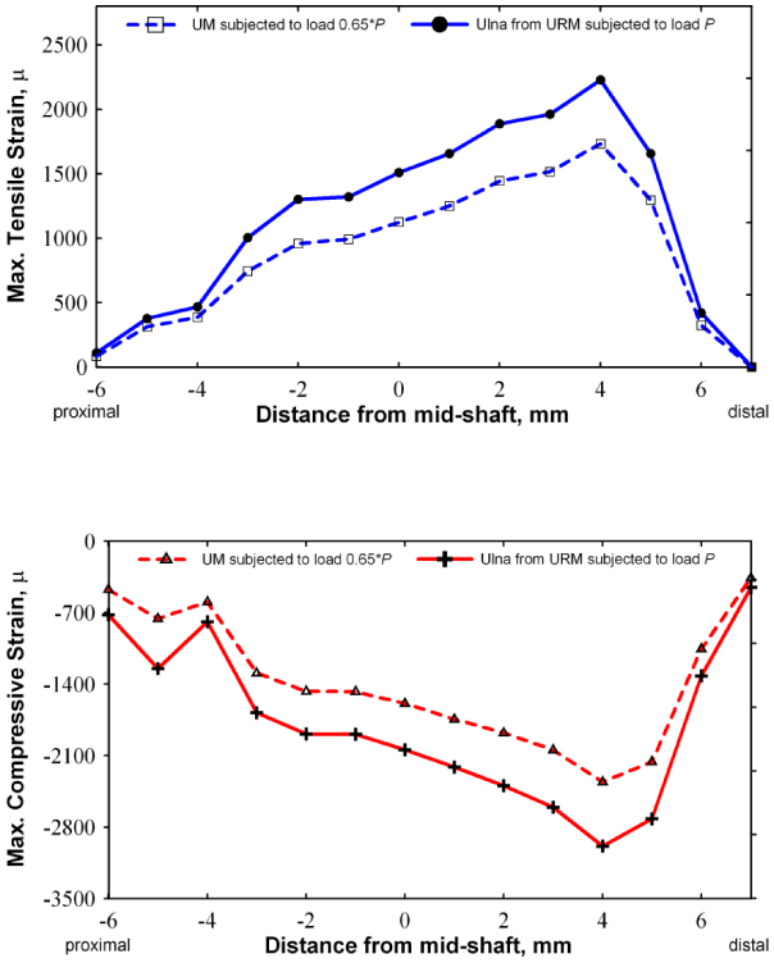

Figure 4.

Graph showing the peak compression and tensile stresses (using 10 node fine mesh) experienced by the ulna at various locations distal and proximal to the mid shaft. For the UM with 1.3 N axial load (represented by the dash lines) and the URM with 2 N axial load (represented by solid line) the maximum tensile and compressive values are shown as separate curves. Higher tensile and compressive strain values can be seen in the URM when compared to the UM.

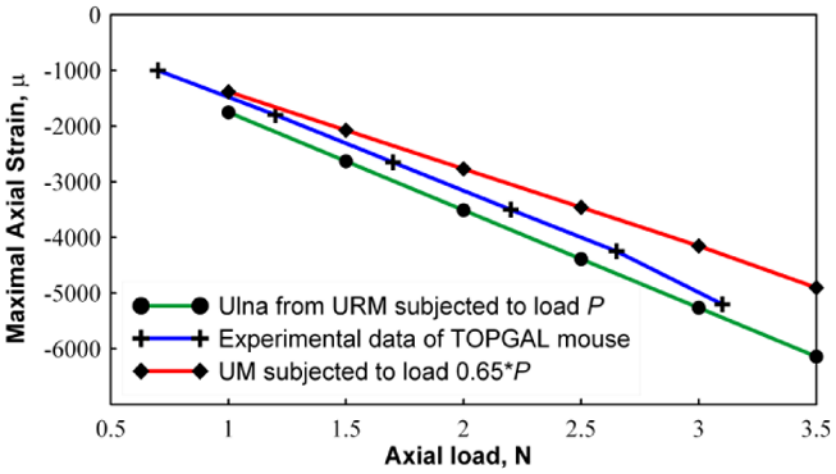

Figure 5.

Graphical representation of the maximum compressive strain (using 10 node fine mesh) at different load magnitudes. Strain values are shown for UM (with 0.65P), URM (with P) and experiments conducted using the mouse forearm. The URM predicts higher compressive strains compared to the experiments in contrast to the UM which predicts lower compressive strains.

Table 1
Comparison of maximum displacement (units: mm)

	ABAQUS		LS-DYNA	
	UM	**URM**	**UM**	**URM**
10-node, coarse mesh	0.1669	0.1352	0.1536	0.1385
10-node, fine mesh	0.1833	0.1554	0.1810	0.1298
4-node, coarse mesh	0.0722	0.0418	0.0861	0.0752
4-node, fine mesh	0.1183	0.0878	0.1436	0.0987

Table 2
Estimated percentage of load shared by ulna (from LS-DYNA)

	Load, N			
Mesh type	**radius**	**ulna**	**total**	**% shared by ulna**
10-node, coarse mesh	0.258	1.768	2.03	87.3%
10-node, fine mesh	0.549	1.358	1.91	71.2%
4-node, coarse mesh	0.266	1.777	2.04	87.0%
4-node, fine mesh	0.686	1.268	1.95	64.9%

Table 3

Maximal axial strain on ulna (units: microstrain)

Model Type	tensile	compressive
UM (with 65% load of 2 N load)	1732	-2356
URM – with 2 N load	2229	-2986